Polyoxometalates RESEARCH ARTICLE

Lanthanide contraction induced coordination-mode transition of phosphotungstate-based complexes for visible-light-driven photocatalytic degradation of ciprofloxacin

Linlin Wang[1,2,§], Yinglong Wang[2,§], Guixiong Guo[2,§], Yu Gao[2], Jinlin Zhai[2], Xiangfu Meng[2], and Qionghua Jin[1,2,3,4,5,6]
[1]*College of Resource Environment and Tourism, Capital Normal University, Beijing 100048, China*
[2]*Department of Chemistry, Capital Normal University, Beijing 100048, China*
[3]*Shanghai Key Laboratory of Chemical Assessment and Pollution Control, Tongji University, Shanghai 200092, China*
[4]*State Key Laboratory of Inorganic Synthesis and Preparative Chemistry, Jilin University, Changchun, 130012, China*
[5]*Key Laboratory of the Ministry of Education for Advanced Catalysis Materials, Zhejiang Normal University, Jinhua 321004, China*
[6]*Jiangxi Province Key Laboratory of Functional Crystalline Materials Chemistry, Jiangxi University of Science and Technology, Ganzhou 341000, China*
[§] *Linlin Wang, Yinglong Wang, and GuiXiong Guo contributed equally to this work.*

Received: 30 July 2026; **Revised:** 25 August 2026; **Accepted:** 2 September 2026

Address correspondence to jinqh204@163.com

Cite This: *Polyoxometalates*, 2027, *6*, 9140159 Read Online

ABSTRACT: Polyoxometalate (POM) based coordination assemblies offer tunable platforms for modulating structural connectivity and photoinduced charge transfer, yet controlled switching of POM between coordinating linkers and non-coordinating counter-anions within a single system remains challenging. Herein, 14 POM-based lanthanide complexes (La-Lu, excluding Pm) were constructed using tetraethyl methylenediphosphonate as an auxiliary ligand. Single-crystal X-ray diffraction reveals a structural transition driven by lanthanide contraction: in complexes **1-4** (La-Nd), the POM coordinates directly to Ln^{3+} centers and bridges two $[LnL_4]^{3+}$ units, whereas in complexes **5-14** (Sm-Lu), it acts as a counter-anion to discrete $[LnL_4]^{3+}$ cations. This switching in coordination mode correlates with distinctly different optical and photocatalytic properties: complexes **1-4** exhibit narrower band gaps (2.94-2.95 eV) and visible-light activity, while complexes **5-14** show wider band gaps (3.22-3.27 eV) and respond mainly to UV light. Complex **1** achieves 94.68% ciprofloxacin degradation within 120 min under visible light ($k = 0.02413\ min^{-1}$), with in situ XPS, EIS, band-structure analysis and in situ EPR collectively supporting photoinduced charge redistribution, improved interfacial charge transport, and generation of $\bullet O_2^-$ and •OH. Meanwhile, complex **6** exhibits a Eu^{3+} centered luminescence lifetime of 3.34 ms and a quantum yield of 29.94%, suggesting radiative relaxation may compete with photocatalytic charge transfer. Collectively, these results support a correlation among lanthanide-contraction-induced coordination-mode transition, POM coordination behavior, and photocatalytic performance, providing a strategy for designing POM-based crystalline functional materials.

KEYWORDS: polyoxometalate, lanthanide contraction, coordination mode switching, photocatalytic, ciprofloxacin

1 Introduction

Polyoxometalates (POMs) occupy an important position in crystalline functional materials because of their well-defined metal-oxygen cluster structures, rich redox properties, and tunable assembly modes [1-4]. In particular, Keggin-type phosphotungstate clusters possess stable inorganic frameworks and good electron-accepting ability, making them attractive building units for hybrid materials related to photoelectric conversion and catalysis [5-7]. However, in POM-based coordination systems, it remains difficult to precisely control whether the POM acts merely as a counter-anion or directly participates in metal coordination as an inorganic building block [8, 9]. Different connection modes of POMs not only determine the crystal structure and packing arrangement of the resulting materials, but also influence electronic communication, interfacial charge transfer, and functional performance between the POM clusters and metal-organic units [10-12]. Therefore, how to regulate the connection or separation between POMs and coordination fragments within the same chemical system remains an important issue in POM structural chemistry and functional material design.

In POM-based lanthanide coordination systems, the cooperative selection of organic ligands and lanthanide metal centers is particularly important for regulating structural assembly. Organic ligands containing phosphoryl oxygen groups possess strong oxygen-donor coordination ability, allowing them to form stable coordination environments with lanthanide ions while providing spatial support and structural regulation between POM clusters and metal-organic fragments [13, 14]. Meanwhile, ligand engineering can also play an important role in charge transfer and photoluminescence behavior in hybrid materials [15]. Lanthanide complexes have also attracted extensive attention in crystalline functional materials owing to their variable coordination numbers, flexible coordination geometries, and unique optical, electrical, and magnetic properties [16]. For systems constructed from POMs, lanthanide metals, and phosphoryl oxygen ligands, whether the terminal oxygen atoms of POMs can further participate in metal coordination depends not only on the oxygen-rich surface of the POM itself, but also on the ligand coordination mode, the spatial environment around the metal center, and the size variation

of lanthanide ions. As the lanthanide series progresses from La to Lu, the ionic size decreases regularly, providing a possible way to observe systematic changes in POM coordination behavior under the same POM, ligand, and synthetic conditions [17, 18]. This also enables further investigation of how the POM connection mode affects crystal structure, light absorption, charge transfer, and photocatalytic reaction processes [19-22].

Previous studies in our group have reported lanthanide-contraction-induced changes in coordination environments and POM binding modes in POM–lanthanide systems [23, 24]. In comparison, the present work provides a more complete POM–lanthanide series from La to Lu (excluding Pm), in which a transition of the POM from direct coordination to counter-anion behavior is observed together with corresponding changes in photoresponse and photocatalytic properties. In this work, a series of lanthanide complexes **1-14** was constructed using phosphotungstic acid (POM), tetraethyl methylenediphosphonate (L) ligand, and lanthanide ions as assembly units. Single-crystal structural analysis shows that, in the La-Nd complexes with larger lanthanide ionic sizes, the terminal oxygen atoms of POM directly coordinate to the lanthanide centers and bridge two [LnL$_4$] units, forming POM-connected structures. In contrast, in the Sm-Lu complexes, as the lanthanide ionic size decreases, the POM clusters no longer enter the first coordination environment of the metal center, but exist as counter-anions, giving ion-separated structures. This series realizes a s ystematic change in the coordination role of POM within the same chemical system, providing a clear model for studying the relationship between POM connection modes and functional properties. Furthermore, PXRD, FT-IR, TGA, BET, SEM, UV-Vis DRS, VB-XPS, EIS, in situ XPS, in situ EPR and photocatalytic degradation experiments using ciprofloxacin as the target pollutant reveal a correlation between the coordination-mode evolution, associated structural variations, and the differences in light absorption, interfacial charge transfer, reactive-species generation, and photocatalytic degradation. [25-32]. This work not only demonstrates an effective strategy for regulating POM connection modes through the continuous variation of lanthanide ions, but also establishes a relationship among coordination-mode transition, optical and charge-transfer properties, and photocatalytic performance, providing new insight into the design of POM-based crystalline functional materials.

2 Experiment

2.1 Materials and synthesis

All chemicals and solvents were commercially available and used without further purification.

As illustrated in Scheme 1, the synthetic routes of lanthanide complexes **1-14**: La(**1**); Ce(**2**); Pr(**3**); Nd(**4**); Sm(**5**); Eu(**6**); Gd(**7**); Tb(**8**); Dy(**9**); Ho(**10**); Er(**11**); Tm(**12**); Yb(**13**); Lu(**14**) are presented. Complex **1** was synthesized as a representative example. A mixture of $LaCl_3{\cdot}6H_2O$ (0.125 mmol), tetraethyl methylenediphosphonate ligand (L, 0.5 mmol), and $H_3PW_{12}O_{40}{\cdot}nH_2O$ (0.125 mmol) was dissolved in a mixed solvent of deionized water (10 mL) and ethanol (30 mL). The resulting solution was stirred and heated at 70 °C for 4 h under reflux. After cooling to room temperature, the solution was filtered and slowly evaporated under ambient conditions for two weeks, yielding colorless block crystals suitable for single-crystal X-ray diffraction (SCXRD) analysis. Complexes **2-14** were prepared using the same procedure by replacing $LaCl_3{\cdot}6H_2O$ with the corresponding lanthanide chloride salts.

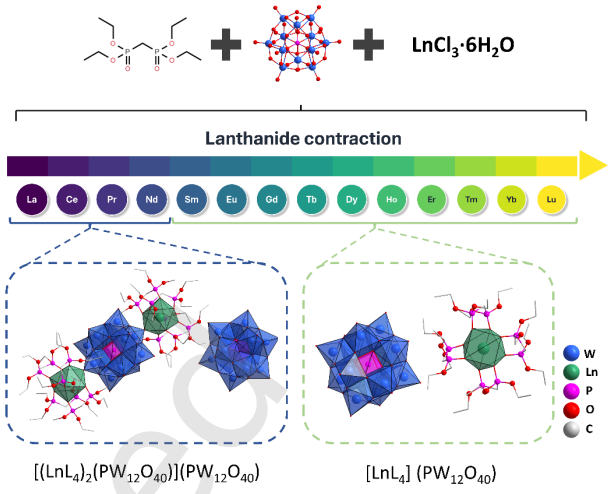

Scheme 1 Schematic Illustration of the Assembly of Complexes **1-14** with Different Coordination Structures Regulated by Lanthanide Contraction.

SCXRD data for complexes **1-14** were collected on a Bruker SMART CCD diffractometer using Mo Kα radiation (λ = 0.71073 Å). The structures were solved by direct methods and refined by full-matrix least-squares methods using the OLEX2/SHELXL program package. Detailed crystallographic parameters and characterization data are provided in the Supplementary Material.

2.2 Photocatalytic experiment

Ciprofloxacin (CIP) was selected as the model pollutant to evaluate the photocatalytic performances of complexes **1-14.** Complex **1** was selected as a representative catalyst for detailed photocatalytic investigations. Typically, 40 mg of catalyst was dispersed in 90 mL of CIP aqueous solution (40 mg L^{-1}). Before irradiation, the suspension was stirred in the dark for 30 min to establish adsorption-desorption equilibrium. The photocatalytic reaction was performed under visible-light irradiation using a 400 W Xe lamp equipped with a 420 nm cutoff filter. At predetermined time intervals, aliquots were collected, centrifuged, and analyzed by UV-vis spectroscopy. The photocatalytic performances of complexes **2-14** were evaluated under identical conditions. Since complexes **5-14** exhibited negligible activity under visible-light irradiation, their photocatalytic properties were further investigated under UV irradiation using a 400 W mercury lamp. Radical trapping experiments were performed by introducing 1 mmol/L EDTA, IPA, and BQ as scavengers for h^+, •OH, and $•O_2^-$, respectively.

3 Results and discussion

3.1 Synthesis and structural overview

Complexes **1-14** were synthesized through the coordination assembly of $H_3PW_{12}O_{40}$ (POM), tetraethyl methylenediphosphonate (L), and $LnCl_3{\cdot}6H_2O$ under mild reflux conditions. Typically, $H_3PW_{12}O_{40}$, L and $LnCl_3{\cdot}6H_2O$ were mixed in an ethanol-water medium with a molar ratio of 1:4:1 and heated at 70 °C under reflux for 4 h, followed by filtration and slow evaporation to afford single crystals. This synthetic system combines the rigid Keggin-type POM anion,

the flexible O-donor L ligand and lanthanide ions in one coordination environment.

The obtained series shows a clear coordination-mode transition governed by lanthanide contraction[33, 34]. For the larger early lanthanides La-Nd, the POM unit participates in coordination and bridges two $[LnL_4]^{3+}$ units, forming POM-bridged complexes formulated as $[(LnL_4)_2(PW_{12}O_{40})]^{3+}$. In contrast, for the smaller later lanthanides Sm-Lu, the POM unit is excluded from the first coordination sphere of Ln^{3+} and remains as a counter-anion, giving ion-separated complexes formulated as $[LnL_4]^{3+}$. Thus, the continuous decrease in Ln^{3+} ionic radius regulates the coordination role of the POM unit, leading to two distinct structural types within the same synthetic system.

Based on rational structural design, the crystal structures of complexes **1**-**14** were systematically resolved and thorough hly analyzed using SCXRD techniques. Furthermore, intermolecular weak interactions were calculated using the PLATON program, revealing well-defined packing arrangements [35].

3.2 Crystal structure

Description of complexes **1-4** $[(LnL_4)_2(PW_{12}O_{40})]$ $(PW_{12}O_{40})$

Since complexes **1-4** share the same structural type and differ only in the central lanthanide ion (Figure S1-4), complex **2** is described here as a representative example. Complex **2** crystallizes in the triclinic crystal system with the space group $P\bar{1}$ (Table 1). Its structure can be formulated as $(CeL_4)_2(PW_{12}O_{40})^{3+}$, in which one POM unit participates in coordination and the other POM unit serves as a counter-anion in the crystal lattice.

In complex **2**, each Ce^{3+} ion is coordinated by oxygen atoms from four L ligands and one oxygen atom from the coordinated POM unit. The four L ligands coordinate to the Ce^{3+} center in a bidentate chelating mode, while the coordinated POM bridges two $[CeL_4]^{3+}$ units through terminal oxygen atoms (Figure 1a). As a result, each Ce^{3+} center is surrounded by nine oxygen atoms, forming a nine-coordinate tricapped trigonal prism mode (Figure 1b).

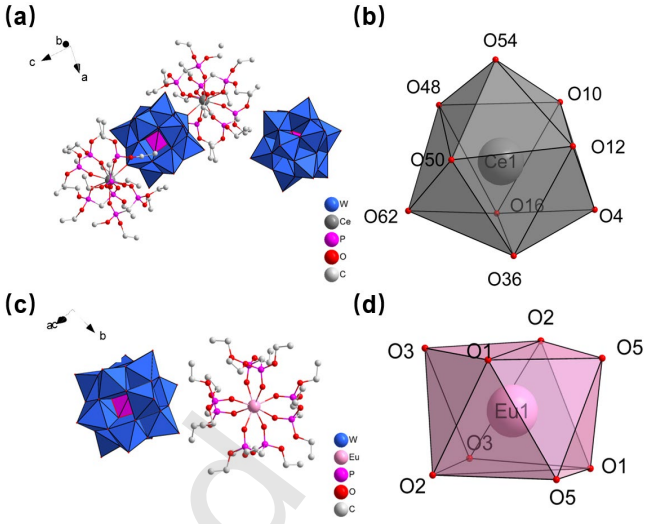

Figure 1 (a) Single-molecular structure of complex **2**; (b) Coordination mode of Ce^{3+} in complex **2**;(c) Single-molecular structure of complex **6**; (d) Coordination mode of Eu^{3+} in complex **6**.

The Ce-O bond lengths range from 2.455 to 2.638 Å, and the selected O-Ce-O bond angles range from 65.9° to 143.4° (Table S3). The crystal packing is further stabilized by multiple intermolecular C-H···O interactions between L and POM, which connect the POM-bridged dinuclear units into an extended supramolecular structure.

As shown in Figure 2a and Table S4, adjacent POM-bridged dinuclear units are first connected through C-H···O interactions, such as C8-H8B···O40 and C29-H29B···O45, forming one-dimensional chain-like assemblies. Viewed along the a axis, these chains are further linked by additional C-H···O contacts, including C13-H13A···O29, C20-H20B···O26, C22-H22A···O56, C21-H21B···O56, C94-H94A···O58, C70-H70A···O45 and C12-H12B···O40, generating a two-dimensional supramolecular layer, as shown in Figure 2b. The layers are subsequently connected through interlayer C-H···O interactions, such as C6-H6A···O15 and C21-H21B···O56, giving a three-dimensional packing structure, as shown in Figure 2c.

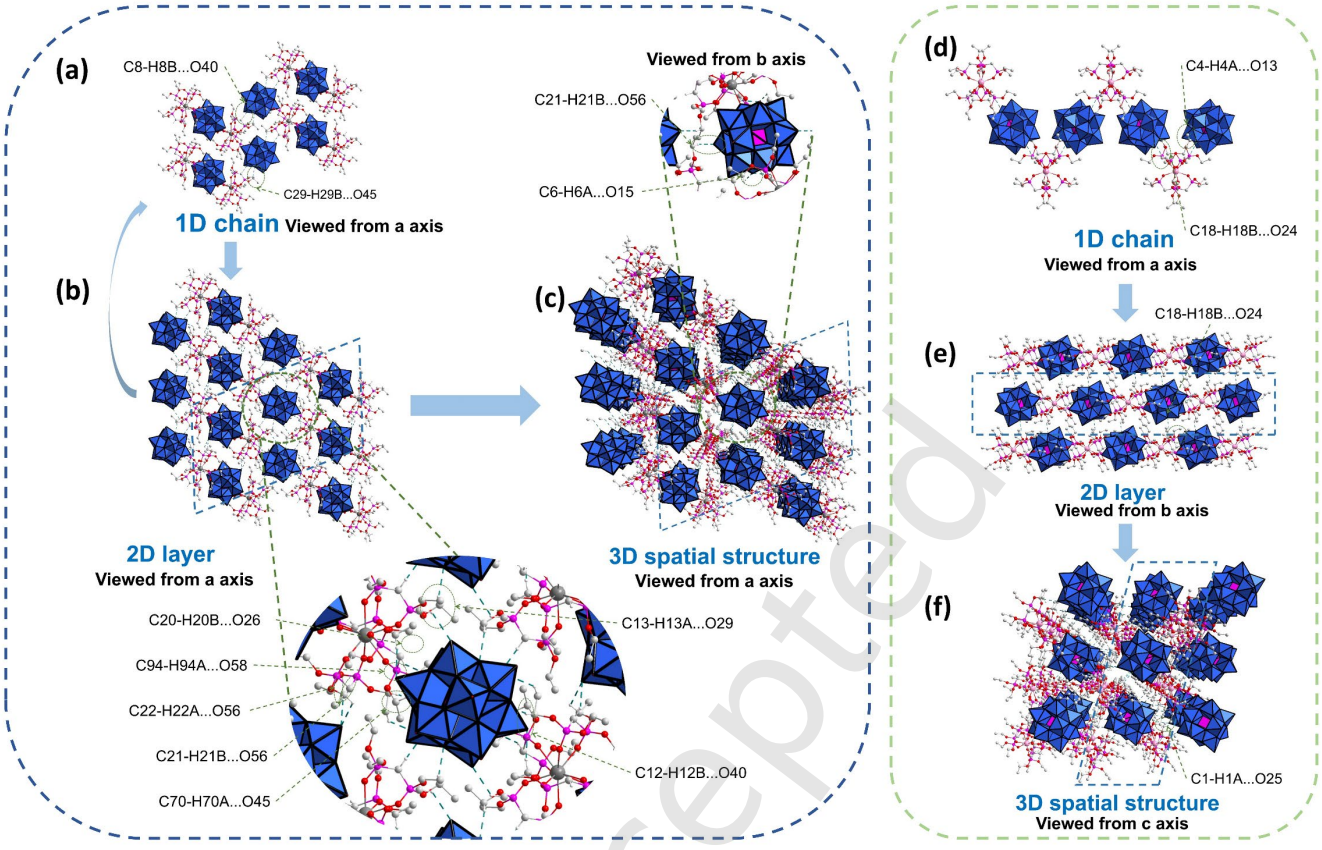

Figure 2 (a) 1D infinite chain structure in complex **2**; (b) 2D supramolecular layer structure in complex **2**; (c) 3D spatial structure in complex **2**; (d) 1D infinite chain structure in complex **6**; (e) 2D supramolecular layer structure in complex **6**; (f) 3D spatial structure in complex **6**.

Description of complexes **5-14** $[LnL_4]$ $(PW_{12}O_{40})$

Since complexes **5-14** share the same structural type and differ only in the central lanthanide ion (Figure S5-14), complex **6** is described here as a representative example. Complex **6** crystallizes in the monoclinic crystal system with the space group C2/c (Table 1). Its structure consists of discrete $[EuL_4]^{3+}$ cations and non-coordinating POM anions.

In contrast to complexes **1-4,** the POM unit in complex **6** does not coordinate to the Eu^{3+} center, but acts as a counter-anion in the lattice (Figure 1a). The Eu^{3+} ion is coordinated exclusively by oxygen atoms from four L ligands. Each L ligand binds to the Eu^{3+} center in a bidentate chelating mode, adopting an eight-coordinate square antiprismatic geometry (Figure 1b). The Eu-O bond lengths range from 2.382 to 2.406 Å, and the selected O-Eu-O bond angles range from 73.2° to 143.5° (Table S3). Intermolecular C-H···O interactions between $[EuL_4]^{3+}$ and POM further connect the ion-separated units into a three-dimensional supramolecular structure.

As shown in Figure 2d and Table S4, the discrete $[EuL_4]^{3+}$ cations and POM anions are initially connected through C-H···O interactions, such as C4-H4A···O25 and C18-H18B···O24, forming one-dimensional chain-like arrangements when viewed along the a axis. These chains are further assembled into two-dimensional layers through additional C-H···O interactions, mainly represented by C18-H18B···O24, as viewed along the b axis in Figure 2e. Finally, the adjacent layers are linked through interlayer C-H···O contacts, such as C1-H1A···O25, resulting in a three-dimensional supramolecular packing structure, as shown in Figure 2f.

As shown in Figure 3a, the average Ln-O bond lengths of complexes **1-14** progressively decrease with decreasing lanthanide ionic radius, following the characteristic lanthanide contraction. A pronounced discontinuity between Nd and Sm coincides with the structural transition from a nine-coordinate POM-bridged motif to an eight-coordinate ion-separated motif. This transition is accompanied by a reorganization of the first coordination sphere around the Ln^{3+} centers. In complexes **1-4**, the POM oxygen atoms participate in the Ln^{3+} coordination environment, whereas in complexes **5-14**, the POM units are excluded from the first coordination sphere and exist as counter-anions. This change reflects an adaptive reorganization of the Ln^{3+} coordination shell along the lanthanide series. With decreasing ionic size, the coordination preference of the Ln^{3+} centers changes, leading to the exclusion of POM oxygen atoms from the primary coordination sphere and the formation of a more compact eight-coordinate environment. Therefore, the observed discontinuity in Ln-O bond lengths is likely associated with the combined effects of the reduced ionic size, altered coordination number, and changes in the local coordination environment. These observations indicate a clear correlation among the lanthanide contraction, coordination-sphere reorganization, and the observed coordination-mode transition.

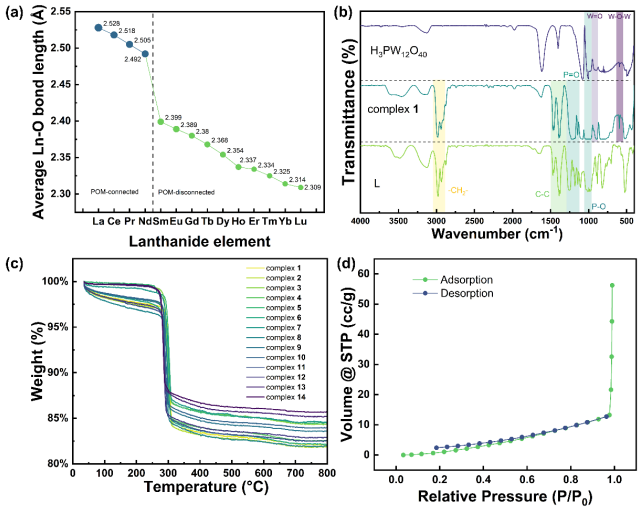

Figure 3 (a) Relationship between Ln^{3+} coordination bond lengths and ionic radii for complexes **1-14**; (b) FT-IR spectra of complex **1**, L and POM; (c) TGA curves of complexes **1-14**; (d) N_2 adsorption-desorption isotherm of complex **1**.

3.3 Structure and property characterization

FT-IR spectroscopy was employed to characterize complexes **1–14** (Figure S15). As shown in Figure 3b, the free L ligand exhibits characteristic absorption bands in the regions of ca. 3000–2900 cm^{-1}, 1450–1350 cm^{-1}, and 1250–950 cm^{-1}, which are assigned to the C-H stretching vibrations of $–CH_2–$ groups and phosphonate-related vibrations, respectively. The parent $H_3PW_{12}O_{40}$ displays the typical characteristic vibrations of the Keggin-type POM anion, with bands located at approximately 1077, 973, 889 and 786 cm^{-1}, corresponding to ν(P–O), ν(W=O), and ν(W–O–W) vibrations, respectively[36]. In complex **1**, the characteristic absorption bands originating from both L and POM components are preserved, while slight shifts and variations in the P–O and W–O vibration regions are observed. These changes indicate the coexistence of ligand and POM units within the framework and are consistent with the coordination interaction between the organic ligand, POM, and lanthanide centers.

Thermogravimetric analysis (TGA) was performed to evaluate the thermal stability of complexes **1-14**. As shown in Figure 3c, all complexes display similar thermal behaviors. Only slight weight loss is observed below ca. 250-280 °C, indicating the absence of a large amount of lattice solvent or weakly bound volatile components. A major weight-loss step occurs at ca. 280-330 °C, which can be assigned to the decomposition of the organic L ligands and the collapse of the coordination framework. After this stage, the remaining mass changes slowly up to 800 °C, giving final residues of approximately 82-86 wt% (Figure S16), consistent with the high inorganic POM content. The comparable TGA profiles suggest that complexes **1-14** possess similar thermal stability, despite the structural transition from the POM-bridged type to the ion-separated type.

N_2 adsorption-desorption measurements were performed on representative complexes **1** and **5** to compare the textural features of the two structural types. Complex **1**, with the POM-bridged structure, shows a higher N_2 uptake and a pronounced increase at high relative pressure, reaching ca. 55-60 $cm^3\ g^{-1}$ near P/P_0 = 1.0. This behavior suggests the presence of more packing-derived textural voids, mainly associated with interparticle spaces and large mesoporous/macroporous voids[37] (Figure 3d). In contrast, complex **5**, with the ion-separated structure, exhibits a much lower N_2 uptake of ca. 8-9 cm^3g^{-1} and a weak hysteresis, indicating fewer interparticle voids and more compact crystal packing (Figure S17). These results support that the coordination-mode transition from the POM-bridged type to the ion-separated type affects the crystal packing and porous textures, although both materials should be regarded as low surface area crystalline complexes rather than typical porous frameworks.

The phase purity of complexes **1-14** was confirmed by powder X-ray diffraction (PXRD). As shown in Figure S18, the experimental PXRD patterns are in excellent agreement with the simulated patterns generated from the single-crystal data, indicating the high phase purity of the bulk samples. The slight differences in peak intensities can be attributed to the preferred orientation of crystallites in the powder samples. The crystal morphologies of complexes **1** and **5** were characterized by SEM (Figure S19).

In situ XPS measurements were performed to investigate the photoinduced electronic evolution of complex **2**. In the W 4f region (Figure 4a), the two fitted W-related components shift from 34.05 and 36.15 eV in the dark to 33.75 and 35.85 eV under light irradiation, corresponding to a negative shift of ca. 0.30 eV. This shift indicates an increased electron density and photoinduced electronic redistribution around the W/POM framework under irradiation, supporting the involvement of the POM unit in the photoinduced charge-transfer process [38]. The accumulated electrons on the W-O framework may further participate in W-centered redox processes and promote electron transfer to dissolved O_2, contributing to reactive oxygen species generation.

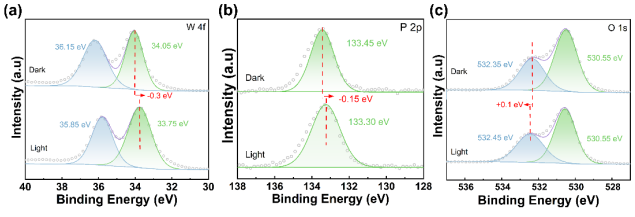

Figure 4 In situ XPS spectra of (a) W4f (b) P 2p (c) O 1s for the complex **2** catalyst under dark and light irradiation conditions.

The P 2p signal also shows a slight negative shift from 133.45 to 133.30 eV after irradiation (Figure 4b). Compared with W 4f, the smaller shift of P 2p indicates that P is not the primary redox-active center, but the P-O environment in the POM/L framework is involved in light-induced charge redistribution. This result is consistent with the electron redistribution suggested by the W 4f spectra.

The O 1s spectra can be divided into two oxygen-related components (Figure 4c). The low binding energy component at 530.55 eV remains nearly unchanged before and after irradiation, indicating that the W-O/W=O oxygen environment in the POM framework is largely preserved. In contrast, the high-binding-energy component shifts slightly from 532.35 to 532.45 eV, suggesting minor electronic modulation of the P-O/P=O/Ln-O/C-O or surface oxygen-related environment. Overall, the in situ XPS results indicate that light irradiation induces charge redistribution mainly around the W/POM framework, while the oxygen

coordination environment remains structurally stable.

3.4 Optical and charge-transfer properties

The optical absorption properties of complexes **1-14** were investigated by UV-Vis DRS. All complexes exhibit strong absorption in the UV region, which is mainly ascribed to the charge-transfer transitions from the occupied states primarily composed of O 2p orbitals to the unoccupied states dominated by W 5d orbitals within the POM units [39]. Some colored lanthanide complexes show weak absorption features in the visible region, and these narrow absorption peaks primarily originate from the 4f-4f inner-shell electronic transitions of the corresponding lanthanide ions (Figure 5a and S20). By employing the direct allowed transition model and extrapolating the linear region of the Tauc plots, the optical band gaps of complexes **1-14** were determined to be 2.95, 2.95, 2.95, 2.94, 3.25, 3.23, 3.27, 3.27, 3.25, 3.25, 3.22, 3.25, 3.25, and 3.24 eV, respectively [40] (Figure 5b and S21). Among them, complexes **1-4** exhibit optical band gaps in the range of 2.94-2.95 eV, corresponding to theoretical absorption edges of approximately 420-422 nm, whereas complexes **5-14** show band gaps of 3.22-3.27 eV, corresponding to absorption edges of approximately 379-385 nm. Therefore, the light-absorption range of complexes **1-4** extends to the UV-Vis border region, whereas complexes **5-14** still predominantly respond to UV light.

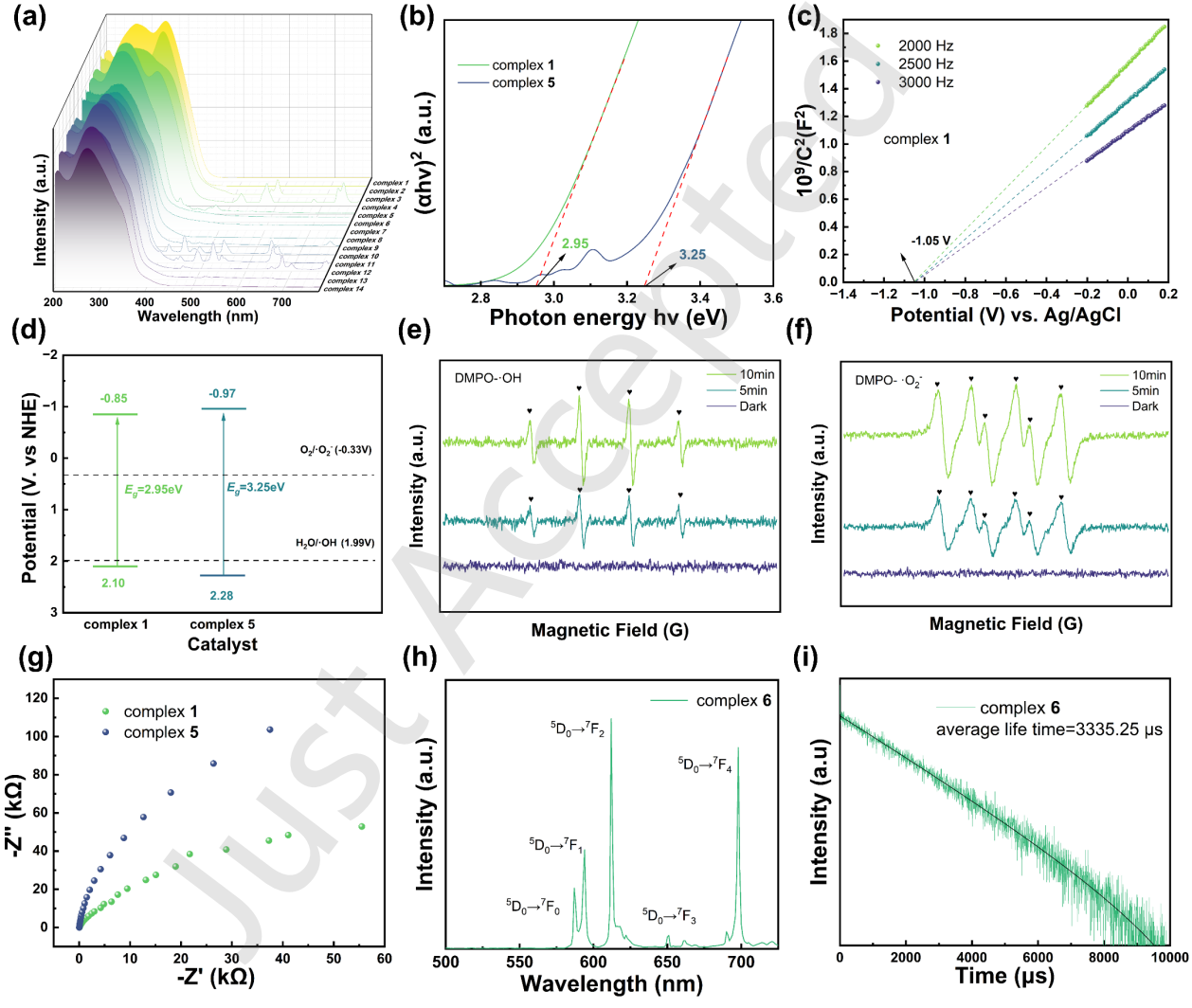

Figure 5 (a) Solid-state (UV-vis DRS) of complexes **1**-**14**; (b)Tauc plot of complex **1** and **5**; (c) Mott-Schottky plots of complex **1**; (d) Band structure diagrams of complex **1** and **5**; (e) In situ EPR spectra of DMPO-•OH adducts for complex **1**; (f) In situ EPR spectra of DMPO-•O_2^- adducts for complex **1**; (g) EIS of complexes **1** and **5**; (h) Emission spectrum of complex **6** (ex = 394 nm); (i) Fluorescence lifetime of complex **6.**

Complexes **1** and **5** were selected as representatives of the two structural types for Mott-Schottky measurements. Both complexes exhibit positive slopes in the Mott-Schottky plots, suggesting their n-type semiconductor characteristics (Figure 5c and S22). The flat-band potentials were obtained from the extrapolated linear regions and were estimated to be -1.05 and -1.17 V vs NHE for complexes **1** and **5**, respectively. Considering that the conduction-band edge of n-type semiconductors is generally slightly more negative than the flat-band potential, the conduction-band positions were estimated according to:

$$E_{CB}=E_{fb}-\Delta E \quad Eq(1)$$

where ΔE represents the correction value (approximately 0.2eV). Combining the obtained conduction-band potentials with the optical band gaps (2.95 and 3.25 eV), the valence-band positions were calculated using:

$$E_{VB}=E_{CB}+E_g \quad Eq(2)$$

The calculated valence-band potentials of complexes **1** and **5** are 2.10 and 2.28 V (vs NHE), respectively, which are close to the VB-XPS measurement results (+2.13 and +2.32 V) (Figure S23). The constructed band structures are shown in Figure 7d. The negative conduction-band potentials are more favorable than the $O_2/\bullet O_2^-$ redox potential (−0.33 V) [41], while the positive valence-band potentials exceed the $OH^-/\bullet OH$ oxidation potential (+1.99 V) [42], indicating that the photogenerated electrons and holes can participate in the generation of $\bullet O_2^-$ and •OH during photocatalysis.

In situ EPR results further corroborate the aforementioned band-structure analysis. Under dark conditions, no appreciable signals were observed for either the DMPO-•OH or DMPO-$\bullet O_2^-$ systems, indicating that virtually no radicals were generated in the absence of light. After 5 min of irradiation, characteristic signals of DMPO-•OH appeared, and the signal intensity further increased when the irradiation time was extended to 10 min, indicating that hydroxyl radicals could be continuously generated during illumination (Figure 5e). Similarly, distinct DMPO-$\bullet O_2^-$ characteristic signals were detected after irradiation, and their intensities increased with prolonged irradiation time from 5 to 10 min, confirming that photogenerated electrons can be transferred to oxygen molecules to generate superoxide radicals (Figure 5f).Therefore, the band-structure analysis and in situ EPR results mutually corroborate each other: the band-edge positions indicate that the system thermodynamically satisfies the conditions for generating $\bullet O_2^-$ and •OH, while in situ EPR directly demonstrates the actual generation of both reactive oxygen species during illumination. The generated $\bullet O_2^-$ and •OH are the key reactive intermediates in the photocatalytic oxidation process.

The Nyquist plots show that complex **1** exhibits a markedly smaller impedance arc than complex **5** (Figure 5g). The smaller semicircular response is associated with a lower interfacial charge-transfer resistance (R_{ct}), indicating more favorable interfacial electron-transfer kinetics in complex **1** [43, 44]. In contrast, the larger impedance arc of complex **5** suggests a higher resistance to interfacial charge transfer and relatively slower electron-transfer kinetics. The reduced charge-transfer resistance of complex **1** facilitates interfacial charge migration and is favorable for the effective utilization and separation of photogenerated charge carriers.

Complex **6** exhibits typical Eu^{3+} characteristic emission. The emission peaks at approximately 594, 612, 650 and 688 nm are attributed to the $^5D_0 \rightarrow {}^7F_1$, $^5D_0 \rightarrow {}^7F_2$, $^5D_0 \rightarrow {}^7F_3$, and $^5D_0 \rightarrow {}^7F_4$ transitions, respectively, among which the $^5D_0 \rightarrow {}^7F_2$ transition at approximately 612 nm is the most intense [45] (Figure 5h). The fitting results of the time-resolved luminescence decay curve indicate that the average luminescence lifetime of complex **6** is 3335.25 μs, i.e., approximately 3.34 ms (Figure 5i).

In addition, complex **6** exhibits an absolute photoluminescence quantum yield (Φ_{PL}) of 29.94%, indicating an appreciable Eu^{3+}-centered radiative decay contribution. This millisecond-scale lifetime corresponds to the luminescent excited-state lifetime of the Eu^{3+} center, suggesting that excitation energy can be efficiently transferred to the Eu luminescent center. The radiative relaxation of the Eu^{3+} center provides a competitive decay channel for the excitation energy, which may reduce the excitation energy available for interfacial charge transfer and reactive oxygen species generation [46].

3.5 Photocatalytic experiment

Using ciprofloxacin (CIP) as the target pollutant, the photocatalytic degradation performances of complexes **1-14** were systematically investigated. Prior to light irradiation, all systems were magnetically stirred in the dark for 30 min to establish adsorption-desorption equilibrium. The dark adsorption results showed that complexes **1-14** exhibited only weak adsorption toward CIP, with dark removal efficiencies of merely 3.6-6.2% (Figure S24-25). These results indicate that the removal of CIP mainly originates from the subsequent photocatalytic degradation process under irradiation rather than from simple adsorption. Therefore, the CIP concentration at the end of the dark adsorption stage was used as the initial concentration for calculating the photocatalytic degradation efficiency, so as to exclude the influence of dark adsorption on the evaluation of photocatalytic performance. Subsequently, all complexes were tested under xenon-lamp visible-light irradiation. As shown in Figure 6a, the POM-connected complexes **1-4** displayed obvious visible-light-driven photocatalytic activity, among which complex **1** showed the highest degradation efficiency, reaching 94.68% after 120 min of irradiation. In contrast, the POM-disconnected complexes **5-14** exhibited almost negligible degradation activity under visible light, with removal efficiencies comparable to those of the isolated POM and the blank system without catalyst. This result indicates a clear correlation between the different structural characteristics of the two groups, including the POM connection mode, and their visible-light response and photocatalytic activity. For complexes **1-4**, the POM-connected architectures, together with their distinct coordination environments and packing features, may contribute to enhanced electronic communication among the POM clusters, lanthanide centers and organic ligands, thereby facilitating photogenerated charge migration and contributing to the improved visible-light-driven degradation efficiency of CIP. [47]. Further comparison of the time-dependent degradation curves of complexes **1-4** shows that all four POM-connected complexes could continuously degrade CIP under visible light irradiation, with the degradation efficiency gradually increasing and then tending to level off as the irradiation time increased (Figure 6b). Complexes **1-4** exhibit similar removal rates, complex **1** showing the highest removal rates. This result further suggests that the structural characteristics of complexes **1-4**, including their POM-connected architecture, are favorable for photogenerated charge transfer and are associated with their higher photocatalytic degradation activity.

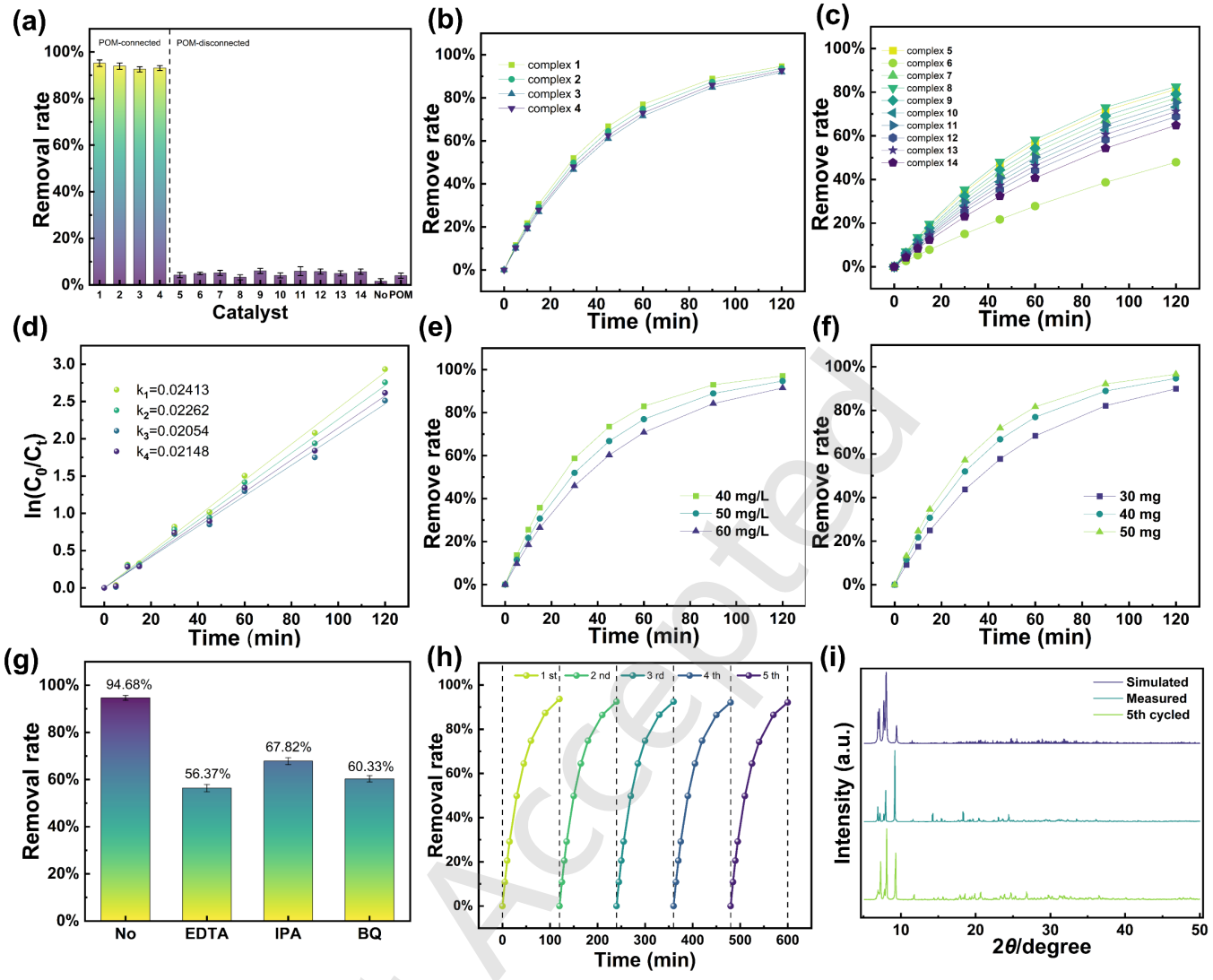

Figure 6 (a) Photocatalytic removal rates of CIP over complexes **1-14**, POM and without catalyst (No) under visible light irradiation; (b) photocatalytic degradation curves of CIP over complexes **1-4** under visible light irradiation; (c) photocatalytic degradation curves of CIP over complexes **5-14** under UV light irradiation; (d) kinetic curves for the photocatalytic degradation of CIP over complexes **1-4** under visible light; (e) visible-light photocatalytic degradation curves of CIP at different concentrations over complex **1**; (f) visible-light photocatalytic degradation curves of CIP with different complex **1** dosages; (g) degradation efficiencies of CIP using different trapping agents over complex **1**; (h) five-cycles stability test of complex **1**; (i) comparison of PXRD simulated, before and after 5th cycled of complex **1**.

Since complexes **5-14** showed almost no effective degradation of CIP under visible light, their photocatalytic performances were further examined under UV irradiation. As shown in Figure 6c, complexes **5-14** exhibited obvious degradation activity toward CIP under UV light, indicating that these POM-disconnected complexes still possess photocatalytic activity, but their effective light absorption and catalytic response mainly occur under higher-energy UV irradiation. Among them, complex **6** displayed the lowest UV-driven photocatalytic degradation efficiency, suggesting that different lanthanide centers and the corresponding structural differences still influence the photocatalytic activity of these POM-disconnected complexes under UV irradiation. Compared with complexes **1-4**, complexes **5-14** lack effective bridging connections between the POM clusters and the lanthanide-organic components, resulting in weaker intercomponent electronic coupling. Consequently, efficient charge separation and migration are difficult to achieve under visible-light irradiation; however, under higher-energy UV excitation, these materials can be effectively activated and thus exhibit certain photocatalytic degradation ability.

To further analyze the reaction kinetics of complexes **1-4** under visible-light irradiation, the CIP degradation data were fitted using a pseudo-first-order kinetic model. As shown in Figure 6d and S26, a good linear relationship between $\ln(C_0/C_t)$ and irradiation time was observed, indicating that the degradation of CIP over complexes **1-4** and **5-14** follows pseudo-first-order kinetics [48-50]. The apparent rate constants of complexes **1-4** were calculated to be 0.02413, 0.02262, 0.02054 and 0.02148 min^{-1}, respectively. Among them, complex **1** possessed the highest apparent rate constant, further confirming that it exhibited the fastest reaction rate and the best visible-light photocatalytic performance in this series.

Using complex **1** as the representative catalyst, the effects of the initial CIP concentration and catalyst dosage on the

degradation performance were further investigated. As shown in Figure 6e and S27, increasing the initial CIP concentration from 40 to 60 mg L^{-1} resulted in a gradual decrease in degradation efficiency. This concentration dependent behavior indicates that the apparent degradation rate is influenced by the initial substrate concentration and does not represent an ideal first-order reaction with a constant rate coefficient. The decrease in apparent activity at higher CIP concentrations may be attributed to enhanced competition between CIP molecules and reactive species, as well as increased occupation of catalytic active sites, which limits the availability of reactive species for CIP oxidation. Similar concentration-dependent variations in apparent kinetic parameters have also been observed in heterogeneous photocatalytic degradation systems. Conversely, increasing the dosage of complex **1** from 30 to 50 mg significantly enhanced the CIP degradation efficiency (Figure 6f and S28), which can mainly be ascribed to the increased number of available active sites and the generation of more photogenerated charge carriers and reactive species under irradiation, thus promoting the oxidative degradation of CIP.

To investigate the reactive species involved in the photocatalytic degradation process, radical trapping experiments were further performed. As shown in Figure 6g, in the absence of scavengers, the degradation efficiency of CIP over complex **1** was 94.68%. After the addition of EDTA, IPA and BQ, the degradation efficiencies decreased to 56.37%, 67.82% and 60.33%, respectively. Since EDTA, IPA and BQ are commonly used as scavengers for h^+, •OH and $•O_2^-$, respectively, the decreased degradation efficiencies suggest that these reactive species contribute to the photocatalytic degradation of CIP. These results are consistent with the in situ EPR observations, which confirmed the generation of radical species under irradiation**.** Among them, EDTA caused the most pronounced inhibition, suggesting that photogenerated holes (h^+) may play a relatively more important role in the degradation process, while $•O_2^-$ and •OH also contribute to CIP oxidation.

The cycling stability of complex **1** is shown in Figure 6h. After five consecutive cycles, complex **1** still maintained a high CIP degradation efficiency, indicating its good reusability. The structural stability of complex **1** before and after photocatalysis was further examined by PXRD. As shown in Figure 6i, the main diffraction peaks of the simulated pattern, the as-synthesized sample and the sample after the fifth cycle are in good agreement, demonstrating that complex **1** can largely retain its crystalline structure after repeated photocatalytic reactions. Therefore, complex **1** not only exhibits excellent photocatalytic activity but also shows good structural stability.

Overall, the POM-connected complexes **1-4** exhibit significantly superior CIP degradation performance under visible-light irradiation compared with the POM-disconnected complexes **5-14**, whereas complexes **5-14** show photocatalytic activity only under UV irradiation. be mainly attributed to the effective intercomponent electronic coup The superior performance of complex **1** is associated with its POM-bridged structural configuration, together with the accompanying coordination environment and packing features, which may collectively contribute to favorable intercomponent electronic coupling, photogenerated charge separation and reactive-species generation. The radical trapping results further confirm that CIP degradation is predominantly driven by h^+, with $•O_2^-$ and •OH acting cooperatively.

3.6 Mechanism investigation

To further elucidate the CIP degradation process in different photocatalytic systems, HPLC-MS analysis was performed using complex **1** under visible light and complex **5** under UV light as representative systems (Figure 7a). In both systems, a series of intermediates were detected at m/z 332, 334, 257, 245, 228, 217, 181, and 127, indicating that CIP undergoes similar stepwise oxidation and cleavage pathways regardless of the photocatalyst type. The m/z 332 signal corresponds to protonated CIP. Initially, reactive species attack the piperazine ring, leading to oxidation, hydroxylation, and ring-opening to generate two isomeric intermediates at m/z 334. These intermediates then convert along two main pathways. In Pathway I, m/z 334 undergoes ring opening and C-N bond cleavage to form m/z 257, which is further oxidized, decarboxylated, and cleaved to yield m/z 217 and then m/z 181. The latter transforms into m/z 127 through defluorination, hydroxylation, and ring cleavage. In Pathway II, m/z 334 undergoes de-piperazination to generate m/z 245, which converts to m/z 228 via deamination and oxidation, ultimately yielding m/z 127. These small molecules may undergo further degradation and mineralization into smaller inorganic products through reactions involving h^+, $•O_2^-$, and •OH. [51-55].

Based on these results, a possible photocatalytic mechanism is proposed (Figure 7b). Upon light irradiation, complexes generate photogenerated electrons and holes. For complexes **1-4**, the POM-connected structure creates close linkages among POM clusters, lanthanide centers, and organic ligands, facilitating electronic communication and carrier separation. Additionally, rich C-H···O weak interactions/hydrogen bonds further connect POM clusters with metal-organic fragments, contributing to close intercomponent contacts and compact supramolecular packing. Such structural features may provide a favorable environment for intercomponent charge transfer. These findings agree with the narrower band gaps of complexes **1-4**, their extended POM to the UV-Vis border, and the lower charge transfer resistance of complex **1**.

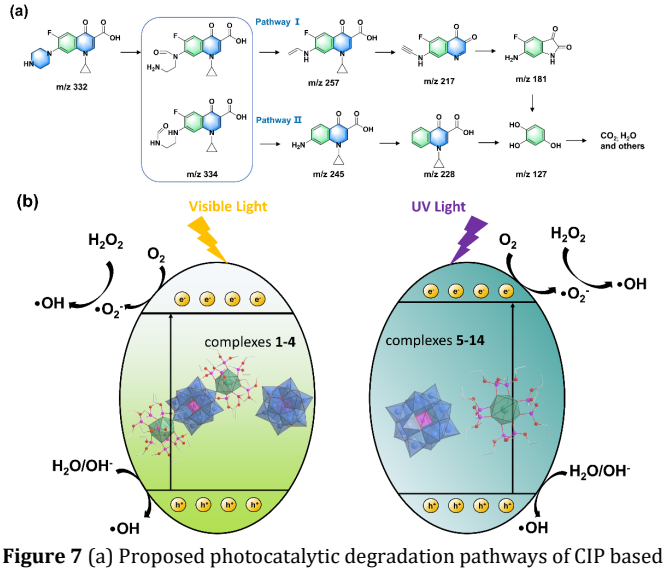

Figure 7 (a) Proposed photocatalytic degradation pathways of CIP based

on the intermediates identified by HPLC-MS. (b) Schematic illustration of the possible photocatalytic degradation mechanism over complexes **1-14** under visible-light and UV-light irradiation.

In situ XPS shows that the W 4f signal shifts negatively upon irradiation, indicating increased electron density around W/POM and supporting photoinduced charge redistribution involving the POM units. Thus, the POM-connected structure, together with the close supramolecular packing associated with the weak-interaction network, may contribute to favorable intercomponent charge-transfer behavior and the enhanced visible-light photocatalytic activity of complexes **1-4**. Upon light irradiation, photogenerated electrons and holes are generated in the complexes. The electrons can reduce dissolved oxygen to generate $\bullet O_2^-$, while photogenerated holes may directly oxidize CIP or react with H_2O/OH^- to produce •OH. In addition, $\bullet O_2^-$ may further participate in secondary oxygen activation processes to generate additional reactive oxygen species. Band structure analysis supports this: the CB potentials are more negative than $O_2/\bullet O_2^-$, and the VB potentials are sufficiently positive for •OH generation. In situ EPR supports the involvement of both radicals, with characteristic DMPO signals appearing upon irradiation and intensifying over time.

For complexes **5-14**, POM units exist as counter-anion rather than being covalently linked to the lanthanide-organic fragments. This ion-separated structure weakens electronic coupling, hindering charge separation under visible light.

Consequently, these complexes show negligible visible-light activity. However, their strong UV absorption and wide band gaps allow excitation under UV light, enabling $\bullet O_2^-$ and •OH generation and thus partial CIP degradation. Complex **6** exhibits the lowest UV activity, which may be partially related to its pronounced Eu^{3+} luminescence. Its millisecond-scale lifetime and characteristic emissions indicate efficient energy transfer to the Eu^{3+} center, where radiative relaxation competes with charge transfer. This competitive relaxation pathway may reduce the excitation energy available for reactive-species generation and thus partially account for its relatively low photocatalytic activity[56]. Therefore, complexes **5-14** are not intrinsically inactive, but their effective photocatalytic response is largely limited to UV excitation. Moreover, strong lanthanide luminescence may consume excitation energy and thus impair photocatalytic efficiency.

4 Conclusions

In summary, fourteen POM-based lanthanide complexes spanning La-Lu (excluding Pm), were successfully synthesized. Lanthanide contraction induces a distinct coordination-mode transition between Nd and Sm. In complexes **1-4**, the POM anion directly coordinates to the Ln^{3+} centers and bridges two $[LnL_4]^{3+}$ units, whereas in complexes **5-14**, it is excluded from the first coordination sphere and exists only as a counter-anion. This coordination-mode transition is accompanied by pronounced changes in the optical and photocatalytic properties. The complexes containing directly coordinated POM units exhibit narrower band gaps and superior visible-light-driven degradation of ciprofloxacin, with complex **1** achieving a removal efficiency of 94.68% within 120 min. Spectroscopic and electrochemical results indicate that the distinct coordination structures, including POM connection modes and the associated coordination environments, are favorable for photoinduced charge redistribution, interfacial charge transport, and reactive-species generation. In addition, complex **6** exhibits characteristic Eu^{3+} centered luminescence, with a lifetime of approximately 3.34 ms and a photoluminescence quantum yield of 29.94%, suggesting that radiative relaxation may compete with photocatalytic charge-transfer processes. Overall, this work demonstrates that lanthanide contraction provides an effective strategy for regulating the coordination role and optical and photocatalytic properties of POM-based crystalline materials, and offers guidance for the future design of structurally tunable photocatalytic and other photo-functional materials through broader combinations of POM clusters, organic ligands, and metal centers.

Electronic Supplementary Material: Supplementary material (including experiment detail; Single-molecular structure; coordination mode; 3D molecular stacking structure of complexes **1-14**;IR spectra; TGA-DTG curve; PXRD; Tacu plot of complexes **1-14**; BET data of complex **5;** SEM of complex **1** and **5;** Photocatalytic experiment) is available in the onlineversion of this article at https://doi.org/10.26599/POM.2026.9140159.

Data availability

The data supporting the findings of this study are available in the Electronic Supplementary Material and from the corresponding author upon reasonable request. CCDC number of complexes **1-14**: 2448002, 2448043 2512697-2512708.

Acknowledgements

This work was supported by Shanghai Key Laboratory of Chemical Assessment and Pollution Control (SCI2025-1); Open Research Fund of Key Laboratory of the Ministry of Education for Advanced Catalysis Materials and Zhejiang Key Laboratory of Advanced Catalysis and Adsorption Materials (KLMEACM202610); Open Project of State Key Laboratory of Inorganic Synthesis and Preparative Chemistry (2026-04); Open Project Program of Jiangxi Province Key Laboratory of Functional Crystalline Materials Chemistry (2024SSY05161).

Declaration of competing interest

The authors have no competing interests to declare that are relevant to the content of this article.

Author contribution statement

Linlin Wang, Yinglong Wang and Guixiong Guo contributed equally to this work. Linlin Wang: Methodology, Formal analysis, Writing - original draft, Visualization, Investigation, Data curation. Yinglong Wang: Methodology, Formal analysis, Writing - original draft, Visualization, Investigation, Data curation. Guixiong Guo: Methodology, Formal analysis, Writing - original draft, Visualization, Investigation, Data curation. Yu Gao: Investigation, Validation. Jinlin Zhai: Software, Formal analysis. Xiangfu Meng: Resources, Data curation. Qionghua Jin: Conceptualization (Lead), Supervision (Lead), Methodology (Lead). All the authors have approved the final manuscript.

Informed consent

Not applicable.

Ethics statement

Not applicable.

Use of AI statement

Writing and polishing grammar

References

(1) Granadeiro, C. M.; Julião, D.; Ribeiro, S. O.; Cunha-Silva, L.; Balula, S. S. Recent advances in lanthanide-coordinated polyoxometalates: from structural overview to functional materials. *Coord. Chem. Rev.* **2023**, *476*, 214914.

(2) Yang, L.; Xu, M.; Wang, H.; Zhang, D.; Zhou, Z. Polyoxometalate-Based Frameworks: Construction Strategies and Photocatalytic Applications. *ChemCatChem* **2024**, *16* (14), e202400006.

(3) Li, L.; Yu, Y.; Hua, Y.; Li, X.; Zhang, H. Recent progress in polyoxometalate-viologen photochromic hybrids: structural design, photochromic mechanism, and applications. *Inorg. Chem. Front.* **2023**, *10* (7), 1965-1985.

(4) Li, L.; Yu, Y.-T.; Zhang, N.; Li, S.; Zeng, J.; Hua, Y.; Zhang, H. Polyoxometalate (POM)-based crystalline hybrid photochromic materials. *Coord. Chem. Rev.* **2024**, *500*, 215526.

(5) Liu, Y.; Tang, C.; Cheng, M.; Chen, M.; Chen, S.; Lei, L.; Chen, Y.; Yi, H.; Fu, Y.; Li, L. Polyoxometalate@Metal-Organic Framework Composites as Effective Photocatalysts. *ACS Catal.* **2021**, *11*, 13374–13396.

(6) Sun, X.; Zhang, J.; Fu, Z. Polyoxometalate Cluster Sensitized with Copper-Viologen Framework for Efficient Degradation of Organic Dye in Ultraviolet, Visible, and Near-Infrared Light. *ACS Appl. Mater. Interfaces* **2018**, *10* (42), 35671-35675.

(7) Boone, M.; Artizzu, F.; Goura, J.; Mara, D.; Deun, R. V.; D'hooghe, M. Lanthanide phosphonate coordination polymers. *Coord. Chem. Rev.* **2023**, *501*, 215525.

(8) Granadeiro, C. M.; de Castro, B.; Balula, S. S.; Cunha-Silva, L. Lanthanopolyoxometalates: From the structure of polyanions to the design of functional materials. *Polyhedron* **2013**, *52*, 10-24.

(9) Korenev, V. S.; Sukhikh, T. S.; Sokolov, M. N. A Series of Lanthanide Complexes with Keggin-Type Monolacunary Phosphotungstate: Synthesis and Structural Characterization. *Inorganics* **2023**, *11* (8), 327.

(10) Song, Y.; Bo, T.; Ma, J.-C.; Ma, J.-F. Highly efficient photoelectrocatalytic degradation for ciprofloxacin with a new polyoxometalate-based metal-organic hybrid/$BiVO_4$ photoanode. *Green Energy Environ.* **2025**, *10* (7), 1531-1542.

(11) Lan, J.; Wang, Y.; Huang, B.; Xiao, Z.; Wu, P. Application of polyoxometalates in photocatalytic degradation of organic pollutants. *Nanoscale Adv.* **2021**, *3* (16), 4646-4658.

(12) Song, H.; Guo, M.-S.; Wang, J.-F.; Liu, Y.-Q.; Bi, H.-X.; Du, J.; An, W.-T.; Ma, Y.-Y.; Han, Z.-G. Reduced phosphomolybdate as photoassisted electrochemical crystalline sensor for trace Cr(VI) detection. *Polyoxometalates* **2024**, *3* (4), 9140065.

(13) Ma, X.-Y.; Bi, H.-X.; Zhang, X.-J.; Du, J.; Ma, Y.-Y.; Han, Z.-G. Effect of bridging units on the detection performance of Cd$\{P_4Mo_6\}^{2-}$based electrochemical sensors for trace chromium(VI) and tetracycline. *Polyoxometalates* **2025**, *4* (2), 9140090.

(14) Guan, Y.; Tang, W.; Zhao, Y.; Li, S.; Wang, L.; Tian, M.; Li, Y.; Chai, F. All-in-one POM-based nanoreactor with oxidase-like activity for versatile detection and antibacterial action. *Polyoxometalates* **2025**, *4* (3), 9140098.

(15) Zeng, Y.; Wu, L.; Luo, J.; Lu, X.; Jia, B.; Liang, L.; Zhang, J. Photocatalytic degradation of ciprofloxacin by Gd-Co/g-C_3N_4 under low-power light source: Degradation pathways and mechanistic insights. *J. Water Process Eng.* **2024**, *58*, 104849.

(16) Zheng, K.; Ma, P. Recent advances in lanthanide-based POMs for photoluminescent applications. *Dalton Trans.* **2024**, *53*, 3949–3958.

(17) Kaledin, A. L.; Yin, Q.; Hill, C. L.; Lian, T.; Musaev, D. G. Ion-pairing in polyoxometalate chemistry: impact of fully hydrated alkali metal cations on properties
of the keggin $[PW_{12}O_{40}]^{3-}$ anion. *Dalton Trans.* **2020**, *49*, 11170–11178.

(18) Platt, A. W. G. Lanthanide phosphine oxide complexe. *Coord. Chem. Rev.* **2017**, *340*, 62–78.

(19) Chen, M.; Yao, J.; Huang, Y.; Gong, H.; Chu, W. Enhanced photocatalytic degradation of ciprofloxacin over Bi_2O_3/$(BiO)_2CO_3$ heterojunctions: Efficiency, kinetics, pathways, mechanisms and toxicity evaluation. *Chem. Eng. J.* **2018**, *334*, 453-461.

(20) Jiao, J.; Zhang, L.; Hu, H.; Sun, H.; Xu, Z.; Pu, Y.; Han, Q. Designing a polyoxometalate-pillared metal-organic framework with long-range delocalization for photocatalytic oxidative cross-coupling. *J. Catal* **2025**, *450*, 116309.

(21) Meng, X.; He, A.; Yan, X.; Wang, L.; Zhao, Z.; Jia, Y.; He, J.; Guo, S.; Shen, H. One-pot gram-scale synthesis of robust copper nanoclusters for photocatalytic difluoroalkylarylation of alkenes. *Polyoxometalates* **2025**, *4* (3), 9140080.

(22) Wang, F.; Jing, C.; Ping, J.; He, D.; Shang, W.; Zeng, M.; Wang, N.; Jia, Z. Polyoxometalate-based Cu(II) complexes as the photocatalyst for oxidation of toluene and photodegradation of metronidazole. *Polyoxometalates* **2024**, *3* (4), 9140067.

(23) Hu, C.; Lu, Y.-L.; Li, Y.-Z.; Yang, Y.-P.; Liu, M.; Liu, J.-M.; Li, Y.-Y.; Jin, Q.-H.; Niu, Y.-Y. Facile high yield, excellent catalytic performance of polyoxometalate-based lanthanide phosphine oxide complexes: Syntheses, structures, photocatalysis and THz spectra. *Environ. Res* **2022**, *206*, 112267.

(24) Li, Y.-Y.; Qiu, Q.-M.; Fan, S.-J.; Xu, J.-J.; Mou, W.-L.; Hou, C.-B.; Liu, M.; Yang, Y.-P.; Dai, L.-X.; Han, H.-L.; Jin, Q.-H. A series of rare-earth phosphine-oxygen complexes containing $[PW_{12}O_{40}]^{3-}$ with highly efficient photocatalytic degradation of MB. *CrystEngComm.* **2024**, *26* (40), 5809-5819.

(25) Jimenez-Salcedo, M.; Monge, M.; Tena, M. T. Study of intermediate by-products and mechanism of the photocatalytic degradation of ciprofloxacin in water using graphitized carbon nitride nanosheets. *Chemosphere* **2020**, *247*, 125910.

(26) Yu, X.; Zhang, J.; Zhang, J.; Niu, J.; Zhao, J.; Wei, Y.; Yao, B. Photocatalytic degradation of ciprofloxacin using Zn-doped Cu_2O particles: Analysis of degradation pathways and intermediates. *Chem. Eng. J.* **2019**, *374*, 316-327.

(27) Zeng, Y.; Chen, D.; Chen, T.; Cai, M.; Zhang, Q.; Xie, Z.; Li, R.; Xiao, Z.; Liu, G.; Lv, W. Study on heterogeneous photocatalytic ozonation degradation of ciprofloxacin by
TiO_2/carbon dots: Kinetic, mechanism and pathway investigation. *Chemosphere* **2019**, *227*, 198–206.

(28) Zhang, H.; Fan, Z.; Chai, Q.; Li, J. Facile Synthesis of a Bi_2WO_6/BiO_{2-x} Heterojunction for Efficient Photocatalytic Degradation of Ciprofloxacin under Visible Light Irradiation. *Catalysts* **2023**, *13*, 469.

(29) Tsai, C.-K.; Huang, C.-H.; Horng, J.-J.; Ong, H. L.; Doong, R.-A. Enhanced Visible-Light-Responsive Photocatalytic Degradation of Ciprofloxacin by the CuxO/Metal-Organic Framework Hybrid Nanocomposite. *Nanomaterials* **2023**, *13* (2), 282.

(30) Liu, Q.; Deng, W.; Zhang, H.; Fang, J.; Xie, Y.; Liu, C.; Han, X.; Xu, X.; Zhou, Z. Enhanced Photocatalytic Activity of CQDs-Modified Layered g-C_3N_4-/Flower-like ZnO Heterojunction for Efficient Degradation of Ciprofloxacin. *Nanomaterials* **2025**, *15* (7), 550.

(31) Si, C.; Liu, X.; Jiao, J.; Xu, J.; Ye, L.; Li, J.; Han, Q. Developing single ligand strategy for engineering a high-performance photocatalyst with the pore space partition and open-metal sites. *Appl. Catal. B Environ. Energy* **2025**, *362*, 124687.

(32) Bi, H.-X.; Ru, H.-H.; Du, J.; Ma, Y.-Y.; Wang, L.-Z.; Han, Z.-G. Tailoring dual-acid sites in lanthanide-incorporated fully reduced phosphomolybdates for the synthesis of polycyclic fused benzodiazepines. *J. Catal.* **2026**, *454*, 116657.

(33) SHANNON, R. D. Revised Effective Ionic Radii and Systematic Studies of Interatomie Distances in Halides and Chaleogenides. *Acta Crystallogr. A* **1976**, *32*, 751–767.

(34) Colliard, I.; Deblonde, G. J. P. Polyoxometalate Ligands Reveal Different Coordination Chemistries Among Lanthanides and Heavy Actinides. *JACS Au* **2024**, *4* (7), 2503-2513.

(35) Spek, A. L. Structure validation in chemical crystallography. *Acta Crystallogr. D* **2009**, *65* (2), 148-155.

(36) ROCCHICCIOLI-DELTCHEFF, C.; THOUVENOT, R.; I~RANCK, R. Spectres i.r. et Raman d'h6t6ropolyanions α-$XM_{12}O_{40}^{n-}$ de structure de type Keggin (X = B ^{III}, Si ^{IV}, Ge ^{IV}, P^{V}, As ^{V}et M=W ^{VI} et Mo ^{VI}). *Spectrochim. Acta A* **1976**, *32*, 587–597.

(37) Thommes, M.; Kaneko, K.; Neimark, A. V.; Olivier, J. P.; Rodriguez-Reinoso, F.; Rouquerol, J.; Sing, K. S. W. Physisorption of gases, with special reference to the evaluation of surface area and pore size distribution (IUPAC Technical Report). *Pure Appl. Chem.* **2015**, *87* (9-10), 1051-1069.

(38) Chen, X.; Wu, H.; Shi, X.; Wu, L. Polyoxometalate-based frameworks for photocatalysis and photothermal catalysis. *Nanoscale.* **2023**, *15* (21), 9242-9255.

(39) Cariño, C.; Proust, A.; Guillemot, G.; K, L.; Blanchard, S.; Gibson, E. A.; Izzet, G. Unveiling photoinduced electron transfers in photosensitized polyoxometalates for solar energy
conversion. *Chem. Sci.* **2025**, *16*, 19493–19518.

(40) Makula, P.; Pacia, M.; Macyk, W. How To Correctly Determine the Band Gap Energy of Modified Semiconductor Photocatalysts Based on UV-Vis Spectra. *J. Phys. Chem. Lett.* **2018**, *9* (23), 6814-6817.

(41) Schneider, J.; Matsuoka, M.; Takeuchi, M.; Jinlong Zhang; Yu Horiuchi; Anpo, M.; Bahnemann, D. W. Understanding TiO_2 Photocatalysis: Mechanisms and Materials. *Chem. Rev.* **2014**, *114*, 9919–9986.

(42) Nosaka, Y.; Nosaka, A. Y. Generation and Detection of Reactive Oxygen Species in Photocatalysis. *Chem. Rev.* **2017**, *117* (17), 11302-11336.

(43) Lazanas, A. C.; Prodromidis, M. I. Electrochemical Impedance Spectroscopy A Tutorial. *ACS Meas. Sci. Au* **2023**, *3*, 162–193.

(44) Yang, L.; Liu, J.; Liu, G.; Xu, N.; Zhang, Z.; Wang, X. A Effectively Sensing Composite Derived From AgNPs and Cu (II)-PMo_{12}-Based Complex:

Electrochemical Detection for Hg^{2+} and Epicatechin. *Appl. Organomet. Chem.* **2026**, *40* (8), e70628.
(45) Thor, W.; Carneiro Neto, A. N.; Moura, R. T.; Wong, K.-L.; Tanner, P. A. Europium(III) coordination chemistry: structure, spectra and hypersensitivity. *Coord. Chem. Rev.* **2024**, *517*, 215927.
(46) John C. de Mello, H.; Wittmann, F. An Improved Experimental Determinationof External Photoluminescence QuantumEfficiency. *Adv. Mater.* **1997**, *9*, 230–232.
(47) Lu, M.; Zhang, M.; Liu, J.; Yu, T.-Y.; Chang, J.-N.; Shang, L.-J.; Li, S.-L.; Lan, Y.-Q. Confining and Highly Dispersing Single Polyoxometalate Clusters in Covalent Organic Frameworks by Covalent Linkages for CO_2 Photoreduction. *J. Am. Chem. Soc.* **2022**, *144* (4), 1861-1871.
(48) Zhu, Q.; An, H.; Xu, T.-Q.; Chen, Y.; Wei, Y.; Sun, H. Polyoxometalates Embedded into Covalent Triazine Frameworks Regulating Charge Transfer for Visible-Light-Driven Synthesis of Functionalized Sulfoxides and Detoxification of Mustard Gas Simulants. *ACS Sustain. Chem. Eng.* **2024**, *12*, 1655–1665.
(49) Makama, A. B.; Salmiaton, A.; Choong, T. S. Y.; Hamid, M. R. A.; Abdullah, N.; Saion, E. Influence of parameters and radical scavengers on the visible-light-induced degradation of ciprofloxacin in ZnO/SnS_2 nanocomposite suspension: Identification of transformation products. *Chemosphere* **2020**, *253*, 126689.
(50) Ahamad, T.; Naushad, M.; Alshehri, S. M. Analysis of degradation pathways and intermediates products for ciprofloxacin using a highly porous photocatalyst. *Chem. Eng. J.* **2021**, *417*, 127969.
(51) Dang, V. D.; Adorna, J.; Annadurai, T.; Bui, T. A. N.; Tran, H. L.; Lin, L.-Y.; Doong, R.-A. Indirect Z-scheme nitrogen-doped carbon dot decorated Bi_2MoO_6/g-C_3N_4 photocatalyst for enhanced visible-light-driven degradation of ciprofloxacin. *Chem. Eng. J.* **2021**, *422*, 130103.
(52) Hu, X.; Hu, X.; Peng, Q.; Zhou, L.; Tan, X.; Jiang, L.; Tang, C.; Wang, H.; Liu, S.; Wang, Y.; Ning, Z. Mechanisms underlying the photocatalytic degradation pathway of ciprofloxacin with heterogeneous TiO_2. *Chem. Eng. J.* **2020**, *380*, 122366.
(53) Salma, A.; Thoroe-Boveleth, S.; Schmidt, T. C.; Tuerk, J. Dependence of transformation product formation on pH during photolytic and photocatalytic degradation of ciprofloxacin. *J. Hazard. Mater.* **2016**, *313*, 49-59.
(54) BAVO DEWITTE, J. D.; DEMEESTERE, K.; VYVERE, V. V. D.; PATRICK DE WISPELAERE; LANGENHOVE, H. V. Ozonation of Ciprofloxacin in Water:HRMS Identification of ReactionProducts and Pathways. *Environ. Sci. Technol.* **2008**, *42*, 4889–4895.
(55) Sun, W.; Geng, X.; Xu, J.; Huang, Y.; Zhong, S.; Lian, L.; Guan, X. Advanced Computational Approaches for Unraveling Transformation Pathways of Organic Micropollutants in Aquatic Environments: Insights from the Photodegradation of Ciprofloxacin. *J. Am. Soc. Mass Spectrom.* **2025**, *36* (7), 1510-1517.
(56) Wei, D.; Huang, Y.; Bai, J.; Seo, H. J. Manipulating Luminescence and Photocatalytic Activities of $BiVO_4$ by Eu^{3+} Ions Incorporation. *J. Phys. Chem. C* **2020**, *124* (22), 11767-11779.